# Electronic Transport Spectroscopy of Carbon Nanotubes in a Magnetic Field

P. Jarillo-Herrero, J. Kong,* H. S. J. van der Zant, C. Dekker, L. P. Kouwenhoven, and S. De Franceschi†

*Kavli Institute of Nanoscience, Delft University of Technology, P.O. Box 5046, 2600 GA Delft, The Netherlands*

(Received 30 September 2004; published 22 April 2005)

We report magnetic field spectroscopy measurements in carbon nanotube quantum dots exhibiting fourfold shell structure in the energy level spectrum. The magnetic field induces a large splitting between the two orbital states of each shell, demonstrating their opposite magnetic moment and determining transitions in the spin and orbital configuration of the quantum dot ground state. We use inelastic cotunneling spectroscopy to accurately resolve the spin and orbital contributions to the magnetic moment. A small coupling is found between orbitals with opposite magnetic moment leading to anticrossing behavior at zero field.

DOI: 10.1103/PhysRevLett.94.156802 PACS numbers: 73.63.Fg, 73.22.-f, 73.23.Hk

The remarkable electronic behavior of carbon nanotubes (CNTs) originates from a particular combination of the symmetry properties of the graphene band structure and the quantization of momentum imposed by periodic boundary conditions along the nanotube circumference [1]. This symmetry results in a fourfold degenerate shell structure in the energy spectrum of CNT quantum dots (QDs). In early experiments on CNT QDs [2,3], however, this symmetry was not observed, presumably due to the presence of defects. Improvements in the quality of CNTs and advances in nanofabrication techniques have enabled the recent observation of fourfold degeneracy in the spectrum of CNT QDs [4,5]. An interesting effect related to the symmetry of the graphene band structure is the modulation of the energy gap in CNTs when placed in a parallel magnetic field, $B$. This effect, predicted early on [6], has only been recently observed in CNT QDs [7,8]. These studies, however, did not show evidence of fourfold symmetry, and the link between the energy spectrum and the $B$ evolution of the QD states was not established.

In this Letter, we report $B$-dependent electronic transport spectroscopy measurements on CNT QDs exhibiting fourfold shell structure. We show the following: (i) each shell consists of two orbitals with opposite magnetic moment; (ii) the splitting of the orbital states with $B$ accounts for all the observed transitions in the spin and orbital configuration of the CNT QD; (iii) a weak coupling exists between orbitals with opposite magnetic moment resulting in level repulsion at $B = 0$; (iv) Zeeman and orbital contributions to the electron magnetic moment can be distinguished by inelastic cotunneling spectroscopy.

The electronic structure of CNTs can be derived from the two-dimensional band structure of graphene. The continuity of the electron wave function around the CNT circumference imposes the quantization of the wave vector component perpendicular to the CNT axis, $k_\perp$. This leads to a set of one-dimensional subbands in the longitudinal direction. Because of symmetry, for a given subband at $k_\perp = -k_0$ there is a second degenerate subband at $k_\perp = k_0$. Figure 1(a) shows in black solid lines the schematic 1D band structure of a gapped CNT near the energy band gap. Both valence and conduction bands have two degenerate subbands, labeled as "+" and "−." Ajiki and Ando [6] predicted that the orbital degeneracy should be lifted by a magnetic field parallel to the CNT axis [Fig. 1(a)]. This effect can be understood by noting that, due to clockwise and anticlockwise motion around the tube, electrons in degenerate + and − subbands should have opposite orbital magnetic moments, $\mu_{\mathrm{orb}}$. In the case of finite length CNTs, a discrete energy spectrum is expected from size quantization. The level spectrum of a CNT QD can then be described as two sets of spin degenerate levels, $E_+^{(n)}$ and $E_-^{(n)}$,

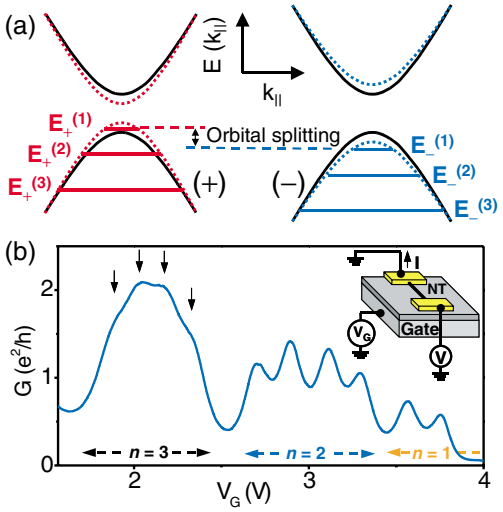


FIG. 1 (color). (a) Schematic band structure of a CNT near its energy gap. Black lines represent the one-dimensional energy dispersion relation, $E(k_\parallel)$, at $B = 0$ ($k_\parallel$ is the wave vector along the CNT axis). The valence (conduction) band has two degenerate maxima (minima). Size quantization in a finite length CNT results in a set of discrete levels with both spin and orbital degeneracy. The degeneracy is lifted by a magnetic field parallel to the CNT. The 1D subbands (and the corresponding levels) at finite $B$ are represented by red and blue dotted (solid) lines. Only the orbital splitting of the energy levels is shown in this figure. (b) Linear conductance, $G$, vs gate voltage, $V_G$, taken at $T = 8$ K. Inset: Device scheme.

 

where $n = 1, 2, 3, \ldots$ is the quantum number in the longitudinal direction [see Fig. 1(a)]. In the absence of intersubband mixing, $E_+^{(n)} = E_-^{(n)}$ at $B = 0$, and a fourfold degenerate shell structure is expected for every $n$. Below we show that a finite coupling can exist, resulting in a small orbital splitting even at $B = 0$.

The fourfold shell filling emerges in a measurement of the linear conductance, $G$, versus gate voltage, $V_G$. This is shown in Fig. 1(b) for a QD device fabricated from a metallic nanotube with a small band gap [7,9,10]. $G$ exhibits Coulomb blockade oscillations [11] corresponding to the filling of the "valence" band of the CNT. From left to right, electrons are consecutively added to the last three electronic shells, $n = 3$, 2, and 1, respectively. The shell structure is apparent from the $V_G$ spacing between the Coulomb oscillations. The addition of an electron to a higher shell requires an extra energy cost corresponding to the energy spacing between shells. This translates into a larger width of the Coulomb valley associated with a full shell [12]. The first group of four Coulomb peaks on the left-hand side of Fig. 1(b) ($n = 3$) is strongly overlapped due to a large tunnel coupling to the leads and the Kondo effect [13]. The coupling decreases with $V_G$, becoming very small near the band gap, which lies just beyond the right-hand side of the $V_G$ range shown [14]. Because of this small coupling, the Coulomb peaks associated with the last two electrons in $n = 1$ are not visible [see Fig. 2(b)].

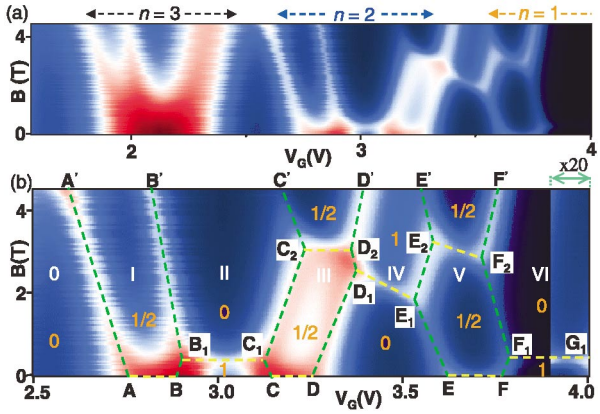


FIG. 2 (color). (a) $G$ vs $B$ on a color scale at $T = 0.34$ K for the $V_G$ range shown in Fig. 1(b). Red, white, and blue indicate high, intermediate, and low $G$, respectively. The conductance range is 0 (dark blue) to $3e^2/h$ (dark red). (b) Zoom-in of (a). Here $G$ ranges from 0 (dark blue) to $2e^2/h$ (dark red). The green dashed lines highlight the evolution of the Coulomb peaks with $B$. They are labeled as $AA'$, $BB'$, ..., $FF'$. These divide the plot in different Coulomb blockade regions indicated by the number of electrons in the last two shells (white numbers 0 to VI). The high-$G$ regions (indicated by yellow dashed lines) in between Coulomb peaks are due to the Kondo effect. Orange numbers indicate the spin in each region. On the right side, the $G$ is multiplied by 20, so that the triplet-singlet transition is clearly seen along $F_1G_1$.

The shell structure breaks up at finite $B$ [Fig. 2(a)]. In each group of four Coulomb peaks, the first (last) two peaks shift towards lower (higher) $V_G$. This behavior demonstrates the strong $B$ dependence of the orbital levels described in Fig. 1(a). The magnetic field shifts the $-$ orbital levels down in energy, while the $+$ orbitals are shifted up due to their opposite $\mu_{\rm orb}$. Consequently, the addition of the first (last) two electrons to a shell results in a pair of Coulomb peaks shifting toward lower (higher) $V_G$. For each shell, $\mu_{\rm orb}$ can be extracted from the shift, $\Delta V_G(n)$, in the position of the corresponding Coulomb peaks. Neglecting the Zeeman splitting, we use the relation $e\alpha\Delta V_G(n) = |\mu_{\rm orb}(n)\cos\varphi\Delta B|$, where $\Delta B$ is the change in $B$, $\varphi$ is the angle between the nanotube and $B$, and $\alpha$ is a capacitance ratio extracted from nonlinear measurements. The values obtained (0.90, 0.80, and 0.88 meV/T,

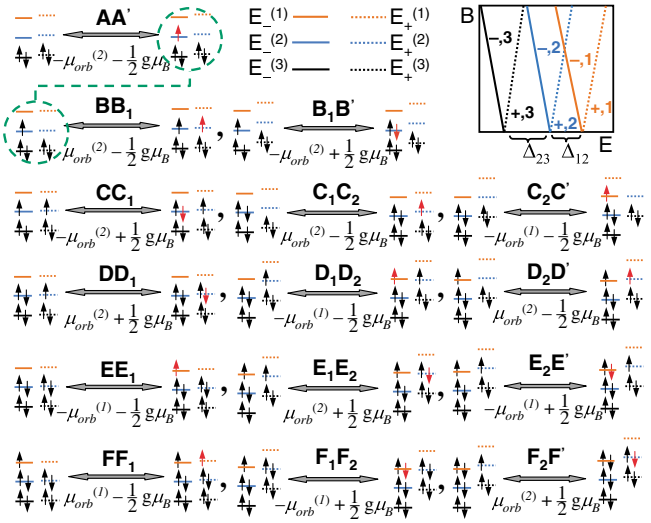


FIG. 3 (color). Diagrams representing the orbital and spin configuration in the different regions of Fig. 2(b). Each row follows the $B$ evolution of a given Coulomb peak. Each section in a given row shows two diagrams (separated by a double arrow). These represent the ground state configuration in the two regions separated by the corresponding segment of the Coulomb peak evolution with $B$. In the diagrams, different colors refer to different shells: orange, blue, and black for $n = 1$, 2, and 3, respectively (in our discussion here, $n = 3$ is always filled). The last added electron is displayed in red, all the others in black. Note that, for each diagram, the final state is the same as the initial state for the diagram immediately below (as indicated by the connected green dashed circles). We use solid (dotted) lines to represent levels with positive (negative) $\mu_{\rm orb}$, shifting down (up) with $B$ (Zeeman splitting is neglected because it is an order of magnitude smaller than the orbital splitting). The slope corresponding to the $B$ evolution of the Coulomb peaks is also indicated under the double arrow. Top right inset: qualitative energy spectrum of the CNT QD as a function of $B$ (Zeeman splitting neglected). Since $\Delta_{1,2} \neq \Delta_{2,3}$, the energy spectrum is not periodic and the $G(B, V_G)$ pattern in Fig. 2 exhibits fourfold symmetry only for $B < 2$T.

for $n = 1, 2$, and 3, respectively) are an order of magnitude larger than the electron spin magnetic moment ($1/2g\mu_B = 0.058$ meV/T for $g = 2$), and in good agreement with an estimate of $\mu_{\rm orb}$ based on the nanotube diameter [15].

The strong $B$ dependence of the orbital states induces changes in the orbital and spin configuration of the QD similar to previous findings in semiconducting QDs [16]. These are reflected as kinks in the evolution of the Coulomb peaks with $B$ [Fig. 2(b)]. Remarkably, a fully consistent description of the $B$-dependent energy spectrum and the ground state spin/orbital configuration can be obtained through a careful analysis of all the kinks in Fig. 2(b), as illustrated by the diagrams in Fig. 3. As an example, we examine the nontrivial evolution of Coulomb peak $CC'$ (notation defined in Fig. 3 caption). Segment $CC_1$ separates the triplet state in region II from the spin $1/2$ state in region III. The incoming electron tunnels into the $E_-^{(2)}$ orbital, with spin down, so the slope of the $CC_1$ segment is "$-\mu_{\rm orb}^{(2)} + 1/2g\mu_B$," as noted underneath the corresponding arrow. At $B_1C_1$, a triplet-singlet transition occurs. Therefore $C_1C_2$ separates the singlet state in region II from the spin $1/2$ state in region III. Now the incoming electron tunnels into the $E_+^{(2)}$ orbital state with spin up, so the slope of $C_1C_2$ is "$\mu_{\rm orb}^{(2)} - 1/2g\mu_B$." Interestingly, at $C_2$ a kink related to an intershell orbital crossing occurs. $C_2C'$ also separates the singlet state in region II from the spin $1/2$ state in region III (as $C_1C_2$), but the incoming electron tunnels into the $E_-^{(1)}$ state and with spin up, so the slope changes direction and has a value "$-\mu_{\rm orb}^{(1)} - 1/2g\mu_B$." The rest of the diagrams can be followed in a similar manner [17].

Note that kinks in Fig. 2(b) are connected by conductance ridges crossing the Coulomb valleys. The enhancement of $G$ at these ridges is due to Kondo effects of different origins. At $B_1C_1$, $D_1E_1$, and $F_1G_1$, the Kondo effect arises from singlet-triplet degeneracy [18]. At $AB$, $CD$, and $EF$, an enhanced Kondo effect is observed in relation to orbital degeneracy [13]. The Kondo ridges at $C_2D_2$ and $E_2F_2$ are due to the recovery of orbital degeneracy between $E_-^{(2)}$ and $E_+^{(1)}$ [13]. Note that, as a result of electron-hole symmetry, region III (three electrons in shell $n = 2$) and region V (one electron in shell $n = 1$) have a certain degree of mirror symmetry, both in terms of the slope of the Coulomb peaks' evolution with $B$ and the Kondo ridges.

The data shown so far have been explained in terms of a $B$-induced splitting of orbital degeneracy, as if the two orbital states of every shell were indeed degenerate at $B = 0$. A small zero-field orbital splitting may in fact exist and be masked by the Kondo effect at $AB$, $CD$, and $EF$. In order to investigate this possibility, we considered a different device, which happened to have a much smaller coupling to the leads and hence a much weaker Kondo effect. This device also exhibits fourfold periodicity in the Coulomb peaks' pattern. Figure 4(c) shows a Coulomb diamond corresponding to one electron in a shell at $B = 80$ mT [19]. Inside the diamond, single electron tunneling is suppressed and transport occurs via higher order cotunneling processes. A sharp increase in the differential conductance, $dI/dV$, is observed at a bias $|V| = V_{\rm in} \sim 190\ \mu$V, denoting the onset of inelastic cotunneling (IC) [20–22]. The IC transition takes place between the two spin degenerate orbital levels of the same shell, thereby indicating the existence of a finite splitting at $B = 0$. Before discussing the $B$ dependence of the IC edges, we note that a weak Kondo peak is also present at $V = 0$ (top inset of Fig. 4(a)]. This Kondo effect arises from the single electron occupancy of the spin degenerate orbital ground state.

At finite $B$, both the Kondo peak and the IC edges split due to Zeeman spin splitting. This is shown in Fig. 4(a), where $dI/dV$ is plotted vs ($V$, $B$) for $V_G$ at the center of the Coulomb diamond [19]. In order to identify the $dI/dV$ steps more clearly, Fig. 4(b) shows the numerical derivative of the $dI/dV$ plot in Fig. 4(a) (i.e., $d^2I/dV^2$ vs $V$ and $B$). IC steps in Fig. 4(a) turn into peaks ($V > 0$) or dips ($V < 0$) in Fig. 4(b). The zero-bias Kondo peak evolves into two $dI/dV$ steps at $V = g\mu_B B/e$ ($g = 2$). These

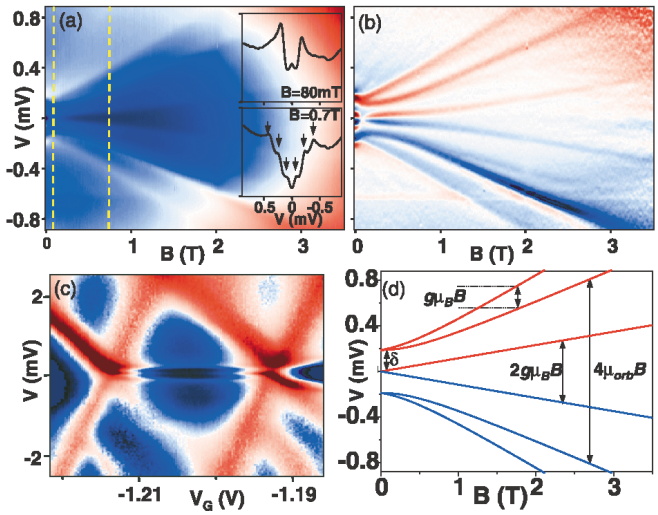


FIG. 4 (color). (a) Color plot of the differential conductance, $dI/dV$, vs bias, $V$, and $B$, measured in the center of the Coulomb diamond [see (c)] at $T = 30$ mK. The yellow dashed lines indicate the traces shown in the top and bottom insets. Insets: (top) $dI/dV$ trace taken at $B = 80$ mT, showing the onset of interorbital IC and a small zero-bias peak due to ordinary spin $1/2$ Kondo effect. The vertical axis scale spans from 0.02 to 0.08 $e^2/h$. (bottom) Same as top inset, but at $B = 0.7$ T, showing the six IC steps. (b) Numerical derivative of the $dI/dV$ plot in (a). The two inner lines result from Zeeman splitting of the Kondo peak at $B = 0$. The outer lines represent the $B$ evolution of the spin-split orbital levels. (c) $dI/dV$ vs $V$ and $V_G$, for a single electron in a shell at $B = 80$ mT. (d) Calculated $B$ dependence of the IC spectrum for a single electron in a spin degenerate level for two coupled orbitals. Red (blue) lines indicate upward (downward) steps in $dI/dV$ with increasing $V$.

correspond to IC processes in which the spin state of the QD is flipped, i.e., from $|-,\uparrow\rangle$ (ground state) to $|-,\downarrow\rangle$ (excited state). Each of the two $dI/dV$ steps associated with interorbital IC splits by $g\mu_B B/e$ and they move further apart due the increasing orbital splitting, $2\mu_{\rm orb}B\cos\varphi$ ($\varphi = 33°$). We estimate $2\mu_{\rm orb} \sim 350\ \mu e$V/T, i.e., $\sim$3 times the Zeeman splitting [23]. The inner interorbital steps correspond to IC from $|-,\uparrow\rangle$ to $|+,\uparrow\rangle$, and evolve with a slope $\pm 2\mu_{\rm orb}/e$. The outer interorbital steps correspond to IC from $|-,\uparrow\rangle$ to $|+,\downarrow\rangle$, and evolve with a slope $\pm(2\mu_{\rm orb} + g\mu_B B)/e$. The six steps (''Zeeman,'' ''orbital,'' and ''orbital + Zeeman'') can be seen in the bottom inset of Fig. 4(a). Such separation between the orbital and Zeeman contributions to the magnetic moment of electrons in CNTs has not been shown before. An important consequence of the angular dependence of the orbital splitting is that researchers have now two ''semi-independent'' knobs to control the energy spectrum of CNT QDs ($B$ controls the Zeeman splitting and the angle nanotube $B$ controls the orbital splitting).

The evolution of the outer IC peaks is nonlinear at low $B$, indicating an anticrossing between the + and − orbital levels. Such IC spectrum can be readily modeled using a Hamiltonian that includes an interorbital coupling besides orbital and Zeeman terms. The corresponding energy eigenstates are $E = \pm\sqrt{(\delta/2)^2 + (\mu_{\rm orb}B\cos\varphi)^2} \pm 1/2 g\mu_B B$ (the four possible sign combinations). The IC spectrum calculated with this simple model [Fig. 4(d)] clearly accounts for the experimental data. The nonlinear evolution of the orbital splitting with $B$ constitutes direct evidence that the so-called ''subband level mismatch,'' usually denoted by $\delta$ [4], is due to a small, but finite, quantum mechanical coupling between the two orbital subbands in carbon nanotubes.

We finally comment on the reproducibility of the results shown. $G(B, V_G)$ patterns with a strong orbital contribution to the magnetic moment of electrons [similar to that in Fig. 2(b)] have been measured in all devices (five from three different fabrication runs) where fourfold shell filling was observed [24]. Our study demonstrates that the spin and orbital configuration of CNT QDs can be understood and controlled by means of a magnetic field. This will prove very useful in a variety of experiments with CNT QDs, such as the study of the Kondo effect in degenerate systems or the interaction between orbital states at high $B$.

Financial support is obtained from the Dutch organization for Fundamental Research on Matter (FOM).

*Present address: Massachusetts Institute of Technology, Cambridge, Massachusetts, USA.

†Present address: Laboratorio Nazionale TASC-INFM, Trieste, Italy.

[1] N. Hamada, S. I. Sawada, and A. Oshiyama, Phys. Rev. Lett. **68**, 1579 (1992).
[2] S. J. Tans *et al.*, Nature (London) **386**, 474 (1997).
[3] M. Bockrath *et al.*, Science **275**, 1922 (1997).
[4] W. Liang, M. Bockrath, and H. Park, Phys. Rev. Lett. **88**, 126801 (2002).
[5] M. R. Buitelaar, A. Bachtold, T. Nussbaumer, M. Iqbal, and C. Schönenberger, Phys. Rev. Lett. **88**, 156801 (2002).
[6] H. Ajiki and T. Ando, J. Phys. Soc. Jpn. **62**, 1255 (1993).
[7] E. Minot *et al.*, Nature (London) **428**, 536 (2004).
[8] U. C. Coskun *et al.*, Science **304**, 1132 (2004).
[9] This band gap can be due to different perturbations, such as curvature or strain. The measured value of the band gap is $\sim$30 meV.
[10] The fabrication is similar to that reported in P. Jarillo-Herrero *et al.*, Nature (London) **429**, 389 (2004).
[11] For reviews, see C. Dekker, Phys. Today **52**, No. 5, 22 (1999); P. L. McEuen, Phys. World **6**, 31 (2000); C. Schönenberger and L. Forro, *ibid.* **6**, 37 (2000).
[12] From measurements in the nonlinear regime (not shown), we estimate $\Delta_{1,2} \sim 3$ meV and $\Delta_{2,3} \sim 5$ meV, where $\Delta_{n,n+1} \equiv E_+^{(n)} - E_+^{(n+1)} = E_-^{(n)} - E_-^{(n+1)}$. The Coulomb charging energy is $U \sim 5$ meV.
[13] P. Jarillo-Herrero *et al.* Nature (London) **434**, 484 (2005).
[14] Ti/Au electrodes typically lead to $p$-doped nanotubes at $V_G = 0$ [see H. T. Soh *et al.*, Appl. Phys. Lett. **75**, 627 (1999)], whose onset of conductance depends on the specific device considered.
[15] From the value for $n = 1$, we extract a nanotube diameter $D = 4\mu_{\rm orb}/ev_F = 4.5$ nm, in agreement with the measured diameter of $4.0 \pm 0.5$ nm as determined by atomic force microscopy. For this device, $\varphi = 37°$.
[16] S. Tarucha, D. G. Austing, T. Honda, R. J. van der Hage, and L. P. Kouwenhoven, Phys. Rev. Lett. **77**, 3613 (1996).
[17] The presence of the Kondo effect causes appreciable shifts in the position of the Coulomb peaks. This accounts for the quantitative discrepancies between the slopes in Fig. 2(b) and those quoted in Fig. 3. To estimate $\mu_{\rm orb}$, we take the average slope between the two Coulomb peaks that correspond to the addition of the electrons to the same orbital state (e.g., $AA'$ and $B_1B'$).
[18] S. Sasaki *et al.*, Nature (London) **405**, 764 (2000).
[19] At $B < 80$ mT, the Ti/Au electrodes become superconducting. The features related to the superconductivity in the contacts [see Figs. 4(a) and 4(b)] will be reported elsewhere.
[20] H. Grabert and M. H. Devoret, *Single Charge Tunneling* (Plenum, New York, 1992).
[21] S. De Franceschi *et al.*, Phys. Rev. Lett. **86**, 878 (2001).
[22] A. Kogan *et al.*, Phys. Rev. Lett. **93**, 166602 (2004).
[23] For this device, the measurements are not taken next to the small band gap, and this is possibly the reason why the value of $\mu_{\rm orb}$ is smaller than expected from the nanotube diameter (2.7 nm) [7] (see also [24]).
[24] Still, in some $V_G$ ranges, the patterns exhibit large variations in $\mu_{\rm orb}$, even for consecutive shells. This might be due to defects, which could distort the band structure enough to render the simple picture in Fig. 1(a) invalid.